nature materials

LETTERS

PUBLISHED ONLINE: 23 NOVEMBER 2015 | DOI: 10.1038/NMAT4479

A new active Li–Mn–O compound for high energy density Li-ion batteries

M. Freire[1,2], N. V. Kosova[3], C. Jordy[2], D. Chateigner[1], O. I. Lebedev[1], A. Maignan[1] and V. Pralong[1]*

The search for new materials that could improve the energy density of Li-ion batteries is one of today's most challenging issues. Many families of transition metal oxides as well as transition metal polyanionic frameworks have been proposed during the past twenty years[1,2]. Among them, manganese oxides, such as the $LiMn_2O_4$ spinel or the overlithiated oxide $Li[Li_{1/3}Mn_{2/3}]O_2$, have been intensively studied owing to the low toxicity of manganese-based materials and the high redox potential of the Mn^{3+}/Mn^{4+} couple. In this work, we report on a new electrochemically active compound with the '$Li_4Mn_2O_5$' composition, prepared by direct mechanochemical synthesis at room temperature. This rock-salt-type nanostructured material shows a discharge capacity of 355 mAh g^{-1}, which is the highest yet reported among the known lithium manganese oxide electrode materials. According to the magnetic measurements, this exceptional capacity results from the electrochemical activity of the Mn^{3+}/Mn^{4+} and O^{2-}/O^{-} redox couples, and, importantly, of the Mn^{4+}/Mn^{5+} couple also.

Positive electrode materials with high energy and power density are important for the next generation of long-life, safety rechargeable lithium-ion batteries, especially for their use in electric and hybrid electric vehicles. As a result, several families of materials have attracted much interest[1–3]. Among the candidates, manganese-based oxides are promising alternatives owing to the voltage range (~2.5–3.6 V) achievable by the Mn^{3+}/Mn^{4+} redox couple, providing low-cost, eco-friendly materials. However, only very few compositions have yet been explored in the Li–Mn–O system. $LiMn_2O_4$ spinel is one of the most important intercalation electrodes at the present time. It exhibits a high operating voltage (4.1 V) with a good rate capability, but suffers from capacity fading at elevated temperatures (>50 °C; refs 4–9). Fortunately, some of the disadvantages of the Li–Mn spinels have been partially overcome, for example, by aluminium substitution[10]. The layered thermodynamically stable, orthorhombic $LiMnO_2$ phase is very attractive from the economic and environmental point of view, but has poor electrochemical activity. The monoclinic Li_2MnO_3 (or $Li[Li_{1/3}Mn_{2/3}]O_2$) exhibits a layered structure and a cation ordering composed of alternating Li^+ and Li/Mn layers, and is electrochemically inactive between 3 and 4 V versus Li^+/Li (refs 11,12). As the second component to Li_2MnO_3, $LiMn_2O_4$ (spinel) or, more often, the layered oxides such as $LiMn_{0.5}Ni_{0.5}O_2$ (ref. 13) or $Li_{1.12}(Ni_{0.425}Mn_{0.425}Co_{0.15})_{0.88}O_2$ (ref. 14) can be used. The most attractive property of the composite electrodes lies in their high reversible capacity (about 200–300 mAh g^{-1}). Several authors have provided evidence that the active redox couple in these composites is related not only to the transition metal, for example, Mn^{3+}/Mn^{4+}, but also to the oxygen couple O^{2-}/O^{-} (refs 15,16). The formation of O_2 at the surface of the material was proposed as an alternative mechanism, leading to the formation of a phase with oxygen vacancies following the cycling process. These new features for the redox process are extremely important for the development of new electrode materials[17,18].

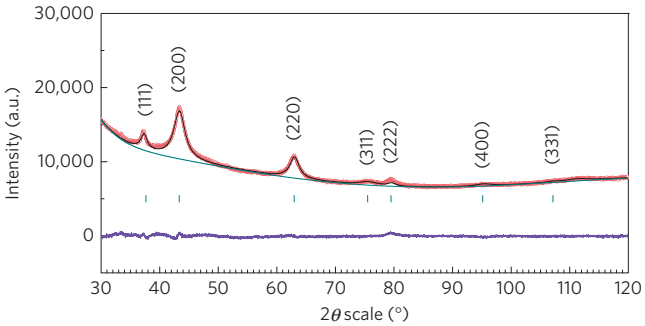

Figure 1 | XRPD analysis. Rietveld-refined XRPD pattern of the '$Li_4Mn_2O_5$' sample using the MAUD software: GoF = 1.53; R_{wp} = 1.58%; R_{Bragg} = 1.23%; $R_{expected}$ = 1.03%.

In addition, nanostructuring is widely used to improve the electrochemical performance of electrode materials. Indeed, according to several reviews[2,19], nanotubes and nanorods have been shown to improve the electrochemical performance of electrode materials, providing higher capacity and better rate capability. In the case of lithium–manganese spinel, nanostructured materials with a mesoporous or nanorod morphology are particularly attractive to enhance their electrochemical properties[20,21]. Because of the relevance of this study, it is worth noting that nanostructured spinel prepared by mechanical activation is characterized by an increased concentration of Mn^{4+} at the surface, preventing manganese dissolution in the electrolyte[22].

In light of these results on the Li–Mn–O system, we have investigated new compositions to determine if we can exceed the capacity of 300 mAh g^{-1} by using a two-electron process (Mn^{3+}/Mn^{5+} redox couple). In this study we report for the first time the synthesis, structural and electrochemical characterizations of a new non-lamellar oxide with the '$Li_4Mn_2O_5$' nominal composition, crystallizing in a rock-salt-type structure and exhibiting the highest capacity ever observed in the Li–Mn–O system.

This phase was prepared by a direct mechanochemical synthesis at room temperature starting from orthorhombic $LiMnO_2$ and Li_2O (2:1 molar ratio) (see Methods). According to X-ray powder diffraction (XRPD), a poorly crystallized material was obtained (Fig. 1) exhibiting strong and anisotropic line broadening. The

[1]Laboratoire de Cristallographie et Sciences des Matériaux CRISMAT, ENSICAEN, Université de Caen, CNRS, 6 Boulevard Maréchal Juin, F-14050 Caen, France. [2]Saft, Direction de la Recherche, 111/113 Boulevard Alfred Daney, 33074 Bordeaux, France. [3]Institute of Solid State Chemistry and Mechanochemistry SB RAS, 18 Kutateladze, Novosibirsk 630128, Russia. *e-mail: valerie.pralong@ensicaen.fr

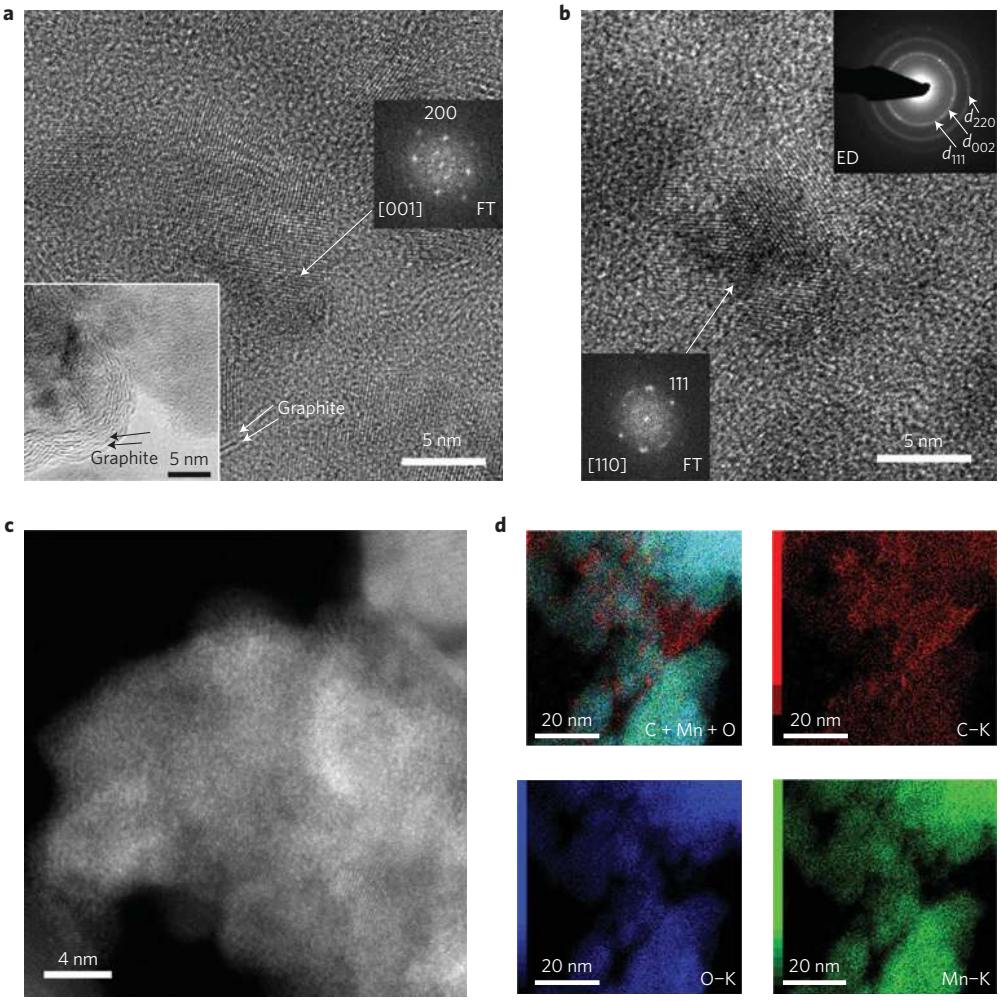

Figure 2 | TEM analyses. a, Bright-field HRTEM image of the '$Li_4Mn_2O_5$' nanoparticles along the [001] zone axis. Notice graphitic layers mixed with nanoparticles marked by white arrows in the main image and black arrows in the bottom left inset. The Fourier-transformed patterns taken from single nanoparticles are given as an inset. **b**, Bright-field HRTEM image of the '$Li_4Mn_2O_5$' nanoparticles along the [110] zone axis. The Fourier-transformed patterns taken from single nanoparticles are given as the bottom left inset. Ring ED pattern is given as the top right inset. **c**, HAADF-STEM image of '$Li_4Mn_2O_5$' samples showing the incorporation of nanoparticles in the carbon matrix. **d**, EDX elemental mapping for the C–K line (red), O–K line (blue) and Mn–K line (green) with an overlay map at the top left showing the distribution of all the elements within the sample.

XRPD pattern of the new material was refined using the Rietveld method and the Popa anisotropic line broadening model[23]. Because of the low X-ray scattering factors of Li, we used a simple rock-salt-type structure within the *Fm*3*m* space group of the MnO phase ($a = 4.16(2)$ Å) as a starting model, in which Mn and O atoms occupy fixed (0, 0, 0) and (1/2, 1/2, 1/2) positions, respectively. The Rietveld refinement obtained with a goodness of fit of only 1.53 indicates that the main heavy atoms of the structure are correctly positioned, with a resulting unit-cell parameter $a = 4.1732(9)$ Å (see Supplementary Figs 1 and 2).

Transmission electron microscopy (TEM) and electron diffraction (ED) studies confirm the nanostructured character of the material. The typical largest crystallite size observed on the images is about 5–10 nm (Fig. 2a). The ring ED pattern can be completely indexed on the basis of the cubic *Fm*3*m* structure with a unit-cell parameter around 4.17 Å obtained by XRPD (Fig. 1). High-resolution TEM (HRTEM) images (Fig. 2a,b) evidence the formation of well-crystallized $Li_4Mn_2O_5$ nanoparticles, which are free from any defects and secondary phases. There is a clear indication of graphitic layers present around the nanoparticles, as evidenced from the HRTEM image in Fig. 2a (see inset) and EDX elemental mapping in Fig. 2d. Moreover, the HAADF-STEM image in Fig. 2c demonstrates that the sample exhibits a mixture of '$Li_4Mn_2O_5$' and carbon material. This is also supported by EDX mapping of nanoparticles (Fig. 2d) showing that the sample consists of homogeneously distributed Mn, O and C (Li is not detectable by EDX). Thus, the TEM image of the '$Li_4Mn_2O_5$' sample and the corresponding ring ED pattern (Fig. 2b) along with the XRPD result (Fig. 1) clearly indicate the monophasic character of the rock-salt-type structure.

The remarkable electrochemical performance of '$Li_4Mn_2O_5$' is shown in Fig. 3. The oxidation process on charging was performed at a rate of one Li^+ in 20 h (C/20) by a gradual increase in the cutoff voltage from 4.4 to 4.6 V and to 4.8 V. Under these conditions, we could completely charge the sample by removing four lithium ions per formula unit (f.u.), as follows from Fig. 3a. The reversible capacity reaches 355 mAh g^{-1} (2.88Li^+/f.u.). It is the highest capacity ever reported among the known lithium manganese electrode materials (see Table 1). Such a high capacity is in principle unexpected, as the oxidation state of Mn ions in $Li_4Mn_2O_5$ is 3+. Then, if one assumes that only the Mn^{3+}/Mn^{4+} redox couple is active, then two Li ions could be extracted, resulting in the formation of $Li_2Mn_2O_5$ with a capacity of 245 mAh g^{-1}.

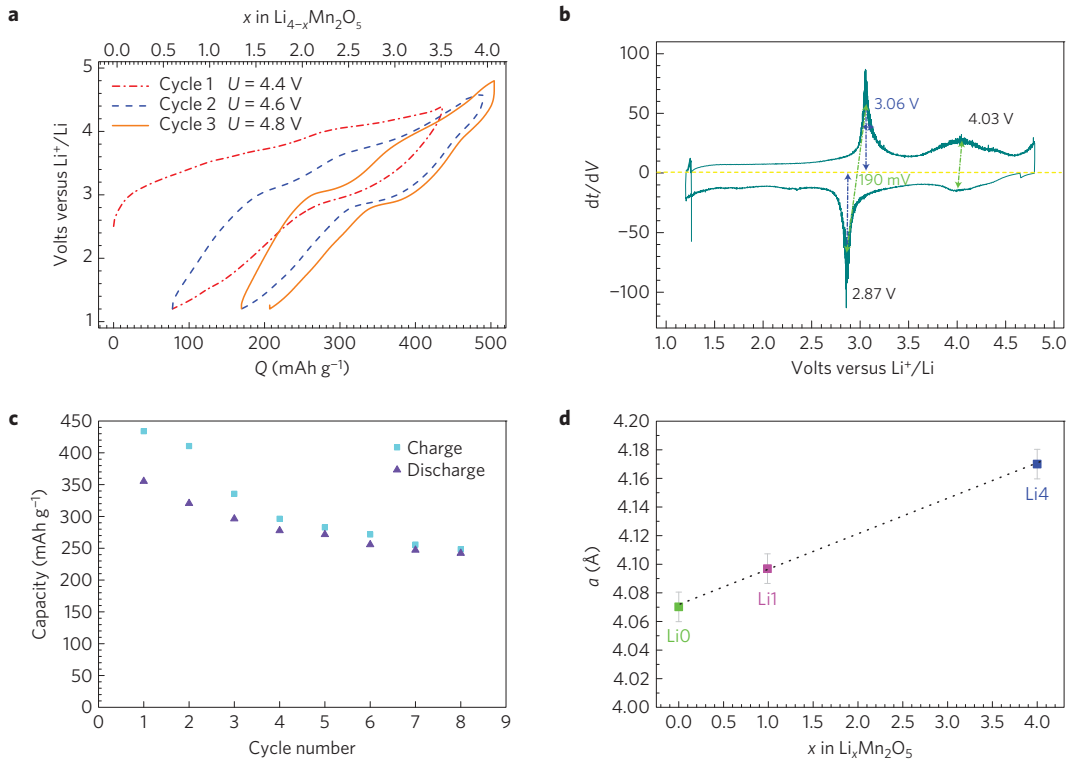

Figure 3 | Electrochemical properties. a, Typical voltage–composition profile of $Li_4Mn_2O_5$ obtained at C/20. **b**, Derivative curve d*t*/d*V* versus voltage for the third cycle. **c**, Discharge capacity versus cycle number of $Li_4Mn_2O_5$. **d**, Evolution of the cell parameters for the Li4, Li1 and Li0 phases.

Table 1 | Comparison in terms of performances, average redox potential and active redox couples for manganese oxides.

Formula	Theoretical capacity (mAh g^{-1})	Experimental capacity (mAh g^{-1}) (C/n)	Experimental average potential (volts versus Li$^+$/Li)	Energy (Wh kg^{-1})	Redox couples	References
$LiMn_2O_4$	148 (1 Li)	120 (C/10)	4.1	572	Mn(3.5+)/Mn(4+)	27
$xLi_2MnO_3\cdot(1-x)LiMO_2$ (M = Mn, Ni)	250 (1 Li)	250 (15 mA g^{-1})	4.5	636	Ni(2+)/Ni(4+)	28
$LiMnO_2$	285 (1 Li)	80–130 (1.37 mA g^{-1})	3	767	Mn(3+)/Mn(3.5+)	29
$Li_{1.20}Mn_{0.54}Co_{0.13}Ni_{0.13}O_2$	378 (1.2 Li)	27 (C/20)	4.0	944	Ni(4+)/Ni(3+)/Ni(2+) Co(4+)/Co(3+) Mn(4+)/Mn(3+) O^{2-}/O^-	15
MnO_2	190 (1 Li)	123 (C/20)	2.8	529	Mn(4+)/Mn(3.5+)	30
$Li_4Mn_2O_5$	492 (4 Li)	355 (C/20)	2.6	953	Mn(3+)/Mn(4+)/Mn(5+) O^{2-}/O^-	This work

Therefore, the electrochemical activity of at least one additional redox couple has to be considered, either Mn^{4+}/Mn^{5+} and/or O^{2-}/O^- and/or O^{2-}/O_2. Indeed, as has been proved previously for the lamellar materials[15,16], oxygen can participate in the electrochemical reactions. Thus, several reactions may occur on charging:

$$Li_4Mn_2^{3+}O_5^{2-} \rightarrow 4Li^+ + 4e^- + Mn_2^{(4-x)+}O_{4-2x}^{2-}O_{2x}^{-}\ (0 \le x \le 1)\ (1)$$

where the redox couples Mn^{3+}/Mn^{4+} and O^{2-}/O^- are involved,

$$Li_4Mn_2^{3+}O_5^{2-} \rightarrow 4Li^+ + 4e^- + Mn_2^{5+}O_5^{2-} \quad (2)$$

where manganese is the only active redox centre (Mn^{3+}/Mn^{4+} and Mn^{4+}/Mn^{5+}),

$$Li_4Mn_2^{3+}O_5^{2-} \rightarrow 4Li^+ + 4e^- + Mn_2^{(5-x)+}O_{5-2x}^{2-}O_{2x}^{-}\ (0 \le x \le 1)\ (3)$$

where three redox couples are involved in the electrochemical process (Mn^{3+}/Mn^{4+}, Mn^{4+}/Mn^{5+} and O^{2-}/O^-), and

$$Li_4Mn_2^{3+}O_5^{2-} \rightarrow 4Li^+ + 4e^- + Mn_2^{(5-x)+}O_{5-2x}^{2-}\square_x + xO_2$$
$$(0 \le x \le 1) \quad (4)$$

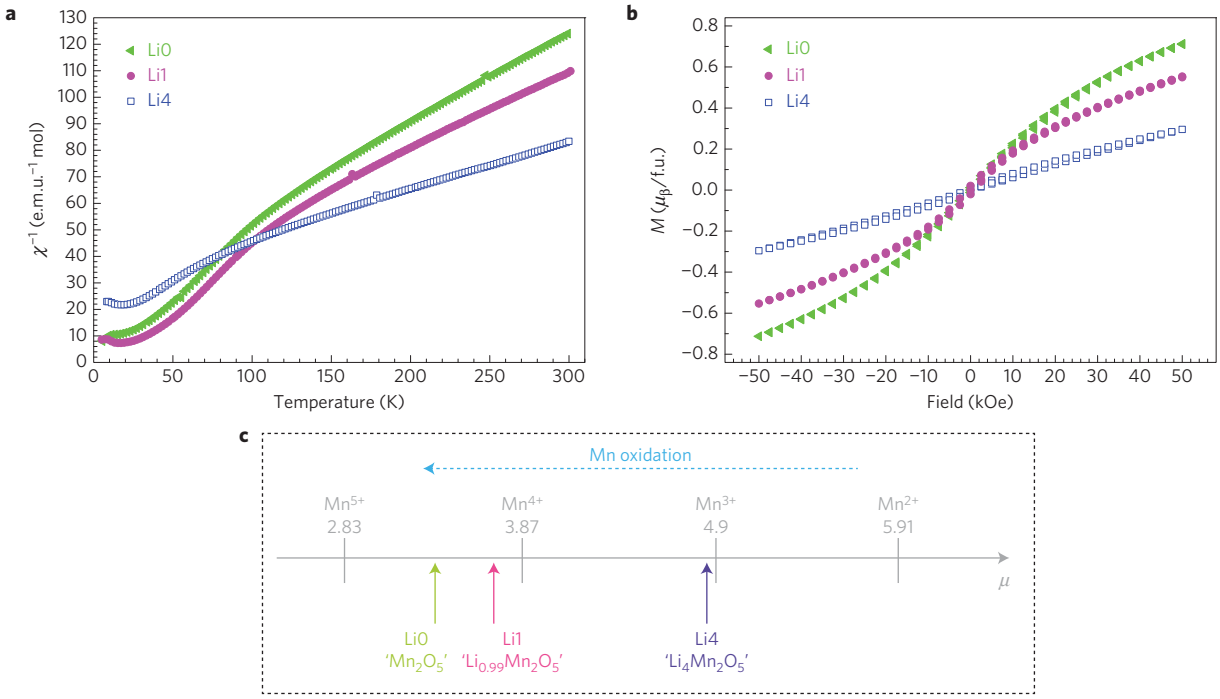

Figure 4 | Magnetic measurements. a, Susceptibility versus temperature for the as-prepared material $Li_4Mn_2O_5$ and partially and fully oxidized samples. **b**, $M(H)$ curves related to these three phases at $T = 5$ K. **c**, Theoretical and experimental paramagnetic effective moments.

where three redox couples are involved in the electrochemical process (Mn^{3+}/Mn^{4+}, Mn^{4+}/Mn^{5+} and O^{2-}/O_2) and □ indicates an oxygen vacancy.

However, under the subsequent cycling, the discharge capacity decreases by up to 250 mAh g^{-1} (after eight cycles; Fig. 3c). On the dt/dV versus voltage plot, one can observe a broad peak centred at 3.06 V versus Li$^+$/Li, which is a characteristic of the Mn^{3+}/Mn^{4+} redox couple, and another peak centred at 4.03 V, which could be ascribed to Mn^{4+}/Mn^{5+} and/or oxygen related redox couples (Fig. 3b and Supplementary Fig. 3).

It is worth noting that the first charge profile differs from the others, and seems to be non-reversible. Charge–discharge curves have a sloping form, suggesting a solid solution process occurs (see Supplementary Fig. 3 for the evolution of CV curves in cycling). This point was further confirmed by *ex situ* XRPD analyses. As shown in Fig. 3d, a linear evolution of the cell parameter from '$Li_4Mn_2O_5$' to 'Mn_2O_5' is observed. Moreover, TEM analysis of the active material after three cycles confirms the rock-salt-type structure is maintained during cycling (see Supplementary Fig. 4).

To gain an insight into the redox couples involved in the lithium process (equations (1)–(4)), magnetic measurements were performed for the three samples: the as-prepared '$Li_4Mn_2O_5$' labelled as Li4, the electrochemically oxidized phase at 4.4 V with the composition of '$LiMn_2O_5$' labelled as Li1, and chemically fully oxidized phase 'Mn_2O_5', labelled as Li0 (see Methods and Fig. 4). In principle, according to the formulae Li4, Li1 and Li0, this system provides a variation of the average oxidation state of manganese ions from Mn^{3+} to Mn^{5+} which can be probed by the extraction of the paramagnetic effective moments from the temperature dependence of the reciprocal magnetic susceptibility $\chi^{-1}(T)$.

A Curie–Weiss-like temperature dependence is observed starting from approximately 100 K up to the highest measured temperature. Table 2 provides information on the magnetism of these samples. The theoretical values of the effective paramagnetic moments, μ_{eff}, for the Li–Mn–O oxides decrease with increasing average oxidation state of the manganese ions in the high-spin state from $\mu_{eff} = 4.89\mu_B/(d^4Mn^{3+}\text{-ion})$ to $\mu_{eff} = 2.83\mu_B/(d^2Mn^{5+}\text{-ion}$; ref. 24).

Table 2 | Magnetic characteristics of the Li4, Li1 and Li0 phases.

Samples	Li4 '$Li_4Mn_2O_5$'	Li1 '$LiMn_2O_5$'	Li0 'Mn_2O_5'
μ_{eff} experimental (μ_B/Mn ion)	4.78 ($Mn^{3.1+}$)	3.68 ($Mn^{4.2+}$)	3.37 if 'Mn_2O_5' according to equation (2) ($Mn^{4.51+}$), 3.31 if '$Mn_2O_{4.4}{}^{2-}O_{0.6}{}^{-}$' according to equation (3)
μ_{eff} theoretical (μ_B/Mn ion)	4.89 (Mn^{3+})	3.38 ($Mn^{4.5+}$)	2.83 (Mn^{5+})
Θ_P (K)	−30.5	−25.5	−20.5

The Curie–Weiss fitting of the $\chi(T)$ curve for 180 K < T < 250 K yields a Curie temperature $\Theta_P = -30.5$ K, which indicates antiferromagnetic spin interactions in the paramagnetic state are in good agreement with the antiferromagnetic state below $T_N \approx 19$ K. For this phase, the calculated effective paramagnetic moment, $\mu_{eff} = 4.78\mu_B$/Mn ion, corresponds to a $Mn^{3.1+}$ oxidation state [$\mu_{eff}(Mn^{3.1+}) = 2[S(S+1)]^{1/2} = 4.78$], which is in agreement with the chemical analysis, and is very close to the effective moment obtained for the $LiMnO_2$ compound[25]. This supports preparation of a compound with all Mn ions in the trivalent state as having been successful.

For the Li1 phase, the high-temperature $\chi(T)$ curve follows a Curie–Weiss behaviour above 100 K, giving $\Theta_P = -25.5$ K and an effective moment $\mu_{eff} = 3.68\mu_B$/Mn ion (Fig. 3a). Such a value corresponds to the manganese oxidation state of 4.2+ (see Table 2). Finally, for the Li0 phase, the Curie–Weiss fitting above 100 K leads to $\Theta_P = -20.47$ K, with an effective moment $\mu_{eff} = 3.37\mu_B$/Mn ion. The latter corresponds to a manganese oxidation state value very close to that of 4.5+ (see Table 2). This μ_{eff} value, far from

the expected value for Mn^{5+} (2.83) in equation (2), suggests the participation of another redox couple (see equations (1) or (4)). At this stage, it is necessary to discuss the possible contribution of a peroxo group in the magnetic curves, as was recently demonstrated for lithium–oxygen cells[26]. Indeed, according to equation (3), the capacity observed at 4.03 V versus Li^+/Li could also be due to peroxo group formation in addition to the Mn^{4+}/Mn^{5+} oxidation. In such a case, according to the capacity calculated from the experimental galvanostatic curve in the potential range 4.0–4.2 V, the fully oxidized phase could be also written as '$Mn_2O^{2-}_{4.4}O^{-}_{0.6}$', which corresponds to $x = 0.3$ in equation (3). Taking into account this formula and adding the magnetic moment of the $S = 1/2$ spin of O^- to that of $Mn^{4.7+}$, a calculated μ_{eff} value of 3.31 μ_B/Mn ion is obtained, which is close to the experimental value, $\mu_{eff} = 3.37\mu_B$/Mn ion. It is important to point out that the manganese oxidation state is 4.7+ in both cases. In addition, magnetic susceptibility studies (see Supplementary Figs 5 and 6) confirm that if Li_2O and $LiMnO_2$ are hypothetically formed after the electrochemical/chemical charge of $Li_4Mn_2O_5$, these decomposition products seem not to have a large impact on the magnetic measurements.

The calculated oxidation states deduced from Curie–Weiss fitting of the macroscopic measurements of magnetic susceptibility were all made by considering the same crystalline field—in particular, high-spin Mn cations in a MnO_6 octahedra. However, even if the coordination for the high-spin 'Mn^{5+}' in the Li0 endmember were to change from MnO_6 octahedra to MnO_4 tetrahedra, according to the orbital configurations, $t_{2g}{}^2e_g{}^0$ (Oc) or $e_g{}^2t_{2g}{}^0$ (Td), both coordinations would lead to $S = 1$ ($\mu_{eff} = 2.82\mu_B$/Mn ion).

Accordingly, the $M(H)$ data at 5 K (Fig. 4b), showing a linear closed-loop characteristic of antiferromagnetism for Li4, is replaced for both Li0 and Li1 by S-shape $M(H)$ curves indicating a more ferromagnetic-like behaviour, with $M(H)$ for Li0 reaching $0.7\mu_B$/f.u. at 5 K—that is, $0.35\mu_B$/Mn.mol. This evolution of the magnetic ordering with the oxidation state of Mn requires neutron diffraction experiments to probe the magnetically ordered structures.

For this magnetic study, it is found that there is a clear evolution of the manganese oxidation state, based on three redox couples.

To summarize, we report on a new electrochemically active compound with the composition of '$Li_4Mn_2O_5$', prepared by direct mechanochemical synthesis at room temperature. It is a rock-salt-type nanostructured material, which shows a discharge capacity of 355 mAh g^{-1}, the highest value ever reported among the known lithium manganese oxide electrode materials. According to the magnetic measurements, the electrochemical activity is due not only to the Mn^{3+}/Mn^{4+} and O^{2-}/O^- redox couples, but also to the Mn^{4+}/Mn^{5+} redox couple.

Methods

Methods and any associated references are available in the online version of the paper.

Received 27 February 2015; accepted 9 October 2015; published online 23 November 2015

References

1. Ellis, B. L. *et al.* Positive electrode materials for Li-ion and Li-batteries. *Chem. Mater.* **22,** 691–714 (2010).
2. Song, H. K. *et al.* Recent progress in nanostructured cathode materials for lithium secondary batteries. *Adv. Funct. Mater.* **20,** 3818–3834 (2010).
3. Tarascon, J. M. Key challenges in future Li-battery research. *Phil. Trans. R. Soc. A* **368,** 3227–3241 (2010).
4. Amatucci, G. *et al.* Optimization of insertion compounds such as $LiMn_2O_4$ for Li-ion batteries. *J. Electrochem. Soc.* **149,** K31–K46 (2002).
5. Thackeray, M. M. *et al.* Structural fatigue in spinel electrodes in high voltage (4V) $Li/Li_xMn_2O_4$ cells. *Electrochem. Solid State Lett.* **1,** 7–9 (1998).
6. Jang, D. H. *et al.* Electrolyte effects on spinel dissolution and cathodic capacity losses in 4 V $Li/LiMn_2O_4$ cells. *J. Electrochem. Soc.* **143,** 2204–2211 (1996).
7. Huang, H. *et al.* Correlating capacity loss of stoichiometric and nonstoichiometric lithium manganese oxide spinel electrodes with their structural integrity. *J. Electrochem. Soc.* **146,** 3649–3654 (1999).
8. Shin, Y. *et al.* Factors influencing the capacity fade of spinel lithium manganese oxides. *J. Electrochem. Soc.* **151,** A204–A208 (2004).
9. Deng, B. H. *et al.* Capacity fading with oxygen loss for manganese spinels upon cycling at elevated temperatures. *J. Power Sources* **180,** 864–868 (2008).
10. Xia, Y. G. *et al.* Improved cycling performance of oxygen-stoichiometric spinel $Li_{1+x}Al_yMn_{2-x-y}O_{4+\delta}$ at elevated temperature. *Electrochim. Acta* **52,** 4708–4714 (2007).
11. Kim, J. S. *et al.* Layered $x LiMO_2 \cdot (1-x)Li_2M'O_3$ electrodes for lithium batteries: A study of $0.95LiMn_{0.5}Ni_{0.5}O_2 \cdot 0.05Li_2TiO_3$. *Electrochem. Commun.* **4,** 205–209 (2002).
12. Kim, J. S. *et al.* Electrochemical and structural properties of $xLi_2M'O_3 \cdot (1-x)LiMn_{0.5}Ni_{0.5}O_2$ electrodes for lithium batteries (M′ = Ti, Mn, Zr; $0 \le x \le 0.3$). *Chem. Mater.* **16,** 1996–2006 (2004).
13. Martha, S. K. *et al.* Surface studies of high voltage lithium rich composition: $Li_{1.2}Mn_{0.525}Ni_{0.175}Co_{0.1}O_2$. *J. Power Sources* **216,** 179–186 (2012).
14. Tran, N. *et al.* Mechanisms associated with the 'plateau' observed at high voltage for the overlithiated $Li_{1.12}(Ni_{0.425}Mn_{0.425}Co_{0.15})_{0.88}O_2$ system. *Chem. Mater.* **20,** 4815–4825 (2008).
15. Koga, H. *et al.* Reversible oxygen participation to the redox processes revealed for $Li_{1.20}Mn_{0.54}Co_{0.13}Ni_{0.13}O_2$. *J. Electrochem. Soc.* **160,** A786–A792 (2013).
16. Sathiya, M. *et al.* Reversible anionic redox chemistry in high-capacity layered-oxide electrodes. *Nature Mater.* **12,** 827–835 (2013).
17. Armstrong, A. R. *et al.* Demonstrating oxygen loss and associated structural reorganization in the lithium battery cathode $Li[Ni_{0.2}Li_{0.2}Mn_{0.6}]O_2$. *J. Am. Chem. Soc.* **128,** 8694–8698 (2006).
18. Kosova, N. V. *et al.* Electronic state of cobalt and oxygen ions in stoichiometric and nonstoichiometric $Li_{1+x}CoO_2$ before and after delithiation according to XPS and DRS. *J. Power Sources* **119–121,** 669–673 (2003).
19. Whittingam, M. S. Inorganic nanomaterials for batteries. *Dalton Trans.* **40,** 5424–5431 (2008).
20. Kim, D. K. *et al.* Spinel $LiMn_2O_4$ nanorods as lithium ion battery cathodes. *Nano Lett.* **8,** 3948–3952 (2008).
21. Kosova, N. V. *et al.* Synthesis of nanosized materials for lithium-ion batteries by mechanical activation. Studies of their structure and properties. *Russ. J. Electrochem.* **48,** 351–361 (2012).
22. Jiao, F. *et al.* Synthesis of ordered mesoporous Li–Mn–O spinel as a positive electrode for rechargeable lithium batteries. *Angew. Chem. Int. Ed.* **47,** 9711–9716 (2008).
23. Popa, N. C. The (*hkl*) dependence of diffraction-line broadening caused by strain and size for all laue groups in Rietveld refinement. *J. Appl. Crystallogr.* **31,** 176–180 (1998).
24. Kittel, C. *Introduction to Solid State Physics 8th Edition* 308 (John Wiley, 2005).
25. Greedan, J. E. *et al.* Long range and short range magnetic order in orthorhombic $LiMnO_2$. *J. Solid State Chem.* **128,** 209–214 (1997).
26. Lu, J. *et al.* Magnetism in lithium–oxygen discharge product. *ChemSusChem* **6,** 1196–1202 (2013).
27. Gummow, R. J. *et al.* Improved capacity retention in rechargeable 4V lithium/lithium–manganese oxide (spinel) cells. *Solid State Ion.* **69,** 59–67 (1994).
28. Kim, D. *et al.* Comments on stabilizing layered manganese oxide electrodes for Li batteries. *Electrochem. Commun.* **36,** 103–106 (2013).
29. Davidson, I. J. *et al.* Lithium-ion cell based on orthorhombic $LiMnO_2$. *J. Power Sources* **54,** 232–235 (1995).
30. Johnson, C. S. Development and utility of manganese oxides as cathodes in lithium batteries. *J. Power Sources* **165,** 559–565 (2007).

Acknowledgements

The authors gratefully acknowledge S. Gascoin for her help in numerous XRPD collections. The authors gratefully acknowledge the CNRS.

Author contributions

M.F., N.V.K. and V.P. contributed to the synthesis of the materials and performed the electrochemical and chemical analysis. M.F. and A.M. performed the magnetic analysis of the samples. D.C. analysed the XRPD data and O.I.L. carried out the TEM analysis. C.J., N.V.K. and V.P. conceived and designed the project. All the authors contributed to writing the paper.

Additional information

Supplementary information is available in the online version of the paper. Reprints and permissions information is available online at www.nature.com/reprints. Correspondence and requests for materials should be addressed to V.P.

Competing financial interests

The authors declare no competing financial interests.

Methods

Materials preparation. The preparation of $Li_4Mn_2O_5$ nanoparticles follows a two-step route, using a mechanochemical activation, which was carried out by means of a Fritsch Planetary Micro Mill PULVERISETTE 7 Premium Line at 700 r.p.m. with a grinding bowl of 20 ml volume made of hard tungsten carbide with four balls (8 mm diameter). First, HT-$LiMnO_2$ was produced by a solid-state reaction method using a reagent mixture of LiOH, MnO_2 and MnO, taken in a 2:1:1 molar ratio, which was ground thoroughly. A small excess (∼5 wt%) of lithium was added to compensate for lithium evaporation at high temperatures. Thereafter, the homogeneous mixture was heat-treated at 1,000 °C under argon flow for 8 h. Then, $LiMnO_2$ was ground with Li_2O (2:1 molar ratio) and 5 wt% of carbon black for a duration of 20 h.

The electrochemically oxidized sample was prepared by the electrochemical oxidation (about three lithium have been extracted from the rock-salt structured '$Li_4Mn_2O_5$' during the charge) at 4.4 V versus Li^+/Li. The fully oxidized sample was prepared by chemical oxidation by means of NO_2BF_4 dissolved in acetonitrile as an oxidizing agent with an equivalent of 5.1 V versus Li^+/Li.

Materials characterization. X-ray powder diffraction (XRPD) patterns were recorded by means of a Bruker D8 diffractometer using Cu Kα1 (1.54056 Å) radiation selected by an incident germanium monochromator, and equipped with a Lynx-Eye detector. The diagrams were collected at room temperature in a continuous scan mode with a step scan of ∼0.011°/2θ ranging from 5 to 120°/2θ. The Rietveld refinement was carried out using the MAUD software. The instrumental contribution was calibrated using a 660 sr mb LaB6 standard from NIST. Line broadening analysis was carried out using the Popa formalism, with harmonic series expansions for crystallite sizes and microstrains with up to four and two coefficients, respectively (expansion order up to $L = 8$ for this Laue group). Transmission electron microscopy (TEM), including electron diffraction (ED), high-resolution TEM (HRTEM) and high-angle annular dark-field scanning TEM (HAADF-STEM) study was carried out on crushed samples in suspension with butanol and deposited on a holey carbon grid in an argon-filled glove box, using a JEM-ARM200F Cold FEG spherical aberration and probe corrected microscope, equipped with a large solid-angle CENTURIO EDX detector and Quantum EELS spectrometer. Taking into account the high sensitivity of the materials to temperature and to avoid destruction of the sample by the e-beam inside the microscope during the TEM measurements, 80 kV conditions have been used. ICP analysis was undertaken with an ICP-AES Varian Vista MPX. The electrochemical performance was tested with Swagelok cells using lithium as a counter electrode. For electrochemical measurements, composite electrodes were made by grinding the '$Li_4Mn_2O_5$' nanopowder with Super P carbon (72:28 by weight). No binder was used, but the positive electrode mixture was pressed to give a good electronic contact between the grains to minimize the cell polarization. The electrolyte was $LiPF_6$ (1 M) dissolved in EC (ethylene carbonate)+EMC (ethyl methyl carbonate) with a volume ratio 3:7. The cells were assembled in an argon-filled dry glove box with a typical loading of 10–15 g cm^{-1} of active material. The electrochemical studies were carried out at room temperature using a VMP II potentiostat/galvanostat (Biologic SA). A slow cycling rate (C/20) was used in a galvanostatic mode between 1.2 V and 4.8 V. The magnetic properties of '$Li_{4-x}Mn_2O_5$' nanopowders (as-prepared, partially and fully oxidized phases) were individually characterized using a MPMS-SQUID magnetometer from Quantum Design, with 40 mg of the sample. The temperature-dependent magnetic moment was measured on warming in 10^{-1}T after a zero-field-cooling process from 300 K. The magnetic susceptibility was calculated by dividing the magnetization by the magnetic field value. The field-dependent magnetic moment values were collected at 5 K.